ADVANCED ENERGY MATERIALS
www.advenergymat.de

Advancing Hematite Photoanodes for Photoelectrochemical Water Splitting: The Impact of g-C_3N_4 Supported Ni-CoP on Photogenerated Hole Dynamics

Mengya Yang, Louise I Oldham, Matyas Daboczi, Yasmine Baghdadi, Junyi Cui, Daniele Benetti, Weilin Zhang, James R Durrant, Anna Hankin, and Salvador Eslava**

The increasing demand for clean hydrogen necessitates the rapid development of efficient photoanodes to catalyze the water oxidation half-reaction effectively. Here a strategy is introduced to fabricate photoanodes that synergistically combine and leverage the properties of porous Ti-doped hematite (Ti-Fe_2O_3) and graphitic carbon nitride (g-C_3N_4) nanosheets anchored with in situ grown Ni-doped CoP co-catalyst (Ni-CoP). The resulting hybrid photoanodes exhibit >7 times higher photocurrent density at +1.23 V_{RHE} compared with Ti-Fe_2O_3 photoanodes. Comprehensive characterization techniques, including ambient photoemission spectroscopy, intensity-modulated photocurrent spectroscopy, and transient absorption spectroscopy complementarily reveal the key impact of g-C_3N_4 in these composites with enhanced solar oxygen evolution reaction: The incorporation of g-C_3N_4 leads to enhanced charge separation through a type-II heterojunction, thereby increasing the hole flux at the surface, and extending the charge carrier lifetime to the ms-s range needed for water oxidation. Additionally, g-C_3N_4 facilitates efficient transfer of photogenerated holes to the fine Ni-CoP nanoparticles confined in the graphitic matrix for a boosted oxygen evolution reaction. These findings highlight the advantages of complex heterostructure photoanodes and demonstrate a new application of g-C_3N_4 as a multifunctional support of co-catalysts for future photoanodes with enhanced performance.

1. Introduction

Solar-driven photoelectrochemical (PEC) water splitting using semiconductor materials represents a clean method for solar energy storage in clean fuels such as hydrogen.[1–4] Among the various semiconductors explored, hematite has attracted considerable attention due to its natural abundance, suitable bandgap in the visible wavelength range (2.0 – 2.2 eV), and long-term chemical stability.[5–7] Theoretically, hematite has the potential to achieve a photocurrent density up to 12.4 mA cm^{-2}.[8,9] However, its practical application is hindered by poor bulk charge carrier mobility, short excited-state lifetime (<10 ps), and sluggish water oxidation kinetics on its surface.[10–12] To address these limitations and improve the efficiency of hematite photoanodes, various strategies have been employed, such as nanostructuring, doping, heterostructure formation, and cocatalyst deposition.[6,13–15] For example, Ti doping adds n-type character and conductivity, improving photocurrents and stability.[16,17] Of particular note is the strategy of enhancing the surface of hematite photoanodes with water-oxidation catalysts, notably group VIII metals (Fe, Co, and Ni) (oxy)hydroxides or phosphides, which has shown promise in enhancing PEC performance.[18–20]

Nonetheless, a key challenge remains in establishing an efficient interface between the photoanode and catalyst, as well

M. Yang, M. Daboczi, Y. Baghdadi, J. Cui, A. Hankin, S. Eslava
Department of Chemical Engineering and Centre for Processable Electronics
Imperial College London
London SW7 2AZ, UK
E-mail: anna.hankin@imperial.ac.uk; s.eslava@imperial.ac.uk

The ORCID identification number(s) for the author(s) of this article can be found under https://doi.org/10.1002/aenm.202401298

DOI: 10.1002/aenm.202401298

L. I Oldham, D. Benetti, J. R Durrant
Department of Chemistry and Centre for Processable Electronics
Imperial College London
London W12 0BZ, UK

W. Zhang
Department of Earth Science and Engineering
Imperial College London
London SW7 2AZ, UK

as in the injection of the electrolyte for water oxidation. Mismatched interfaces between hematite and catalyst, which may serve as charge recombination centers, hamper the charge transfer and injection despite the otherwise good performance of the catalyst.[21] Addressing this issue requires the development of facile and efficient approaches to create high-performing catalyst-modified hematite photoanodes. One precise approach involves introducing a heterojunction interface. For example, a crystalline α-Fe_2O_3/Fe_2TiO_5 heterojunction improves charge separation and PEC response due to improved charge separation driven by more favorable band alignment.[22] Moreover, p-type NiO forms a p-n junction, which aids charge transport, separation, and oxygen evolution.[23] Similarly, a Co_3O_4-modified p-n junction of $CaFe_2O_4$/α-Fe_2O_3 can reduce recombination, resulting in a five-fold increase in PEC response at +1.23 V_{RHE} compared with bare α-Fe_2O_3, and a negative onset potential shift to +0.6 V_{RHE}. Co_3O_4 can serve a dual role, passivating the surface and enhancing water oxidation kinetics.[24] The effects of these heterojunctions have been mainly centered on facilitated charge separation and band bending. However, their impact on charge carrier dynamics, especially in maintaining photoinduced holes on the ms-s timescale required for the oxygen evolution reaction (OER), is still not well explored. In this context, transient absorption spectroscopy (TAS) has been shown to be a powerful technique to investigate how cocatalysts can influence the lifetime of hole populations in semiconducting photoanodes. For example, TAS demonstrated that the addition of Co–Pi co-catalyst on hematite can extend hole lifetimes to the ms-s timescale by reducing back electron/hole recombination, thereby facilitating a more efficient OER.[25] Despite this progress, fabricating high-performing catalyst-modified hematite photoanodes yielding the long-lived holes required for OER function is still a crucial challenge.

Recently, there has been much attention focused on 2D g-C_3N_4 (CN) nanosheets owing to their high thermal and chemical stability caused by their polymeric nature consisting of C, N, and some impurity H, connected via tris-triazine-based patterns, and CN exhibits visible light absorption with a bandgap of ≈2.7 eV.[26–28] These properties make CN a good candidate for constructing heterostructures with other semiconductors to enhance charge carrier separation, lifetime of photogenerated charge carriers, and light utilization. These properties have been widely exploited in the formation of photocatalytic composites such as Z-scheme heterojunctions, but remain poorly explored in photoelectrodes along with its impact on charge carrier dynamics.[29,30] Additionally, the nanosheet structure of CN provides a unique platform of large accessible surfaces for supporting small catalytic particles, and even single-atom catalysts, without aggregation, offering control over morphology, structure, number of active sites, and mass transfer.[31,32]

In this work, we investigate the effect of anchoring ultrafine catalytic Ni-doped cobalt phosphide (NCP) nanoparticles on CN nanosheets and incorporating them onto hematite photoanodes to boost their PEC performance. The resulting photoanodes, consisting of porous nanostructured Ti-doped hematite (Ti-Fe_2O_3) coated with CN-supported NCP nanoparticles (Ti-Fe_2O_3/CN/NCP), deliver a high photocurrent density of 2.01 mA cm^{-2} at +1.23 V_{RHE}, compared with 0.28 mA cm^{-2} at +1.23 V_{RHE} of the Ti-Fe_2O_3 photoanode. Techniques such as ambient photoemission spectroscopy (APS), intensity-modulated photocurrent spectroscopy (IMPS), and bias-dependent TAS, show that CN serves as a high surface area support that facilitates the dispersion and stabilization of small, 10-nm size NCP nanoparticles for more efficient catalysis. Furthermore, CN/NCP passivates recombination surface states on hematite and forms a hematite/CN type-II heterojunction that boosts charge transfer and separation, and accumulation for enhanced charge dynamics and catalysis. These findings and the revealed mechanisms emphasize the benefits of using CN as catalyst support for photoanodes, providing an efficient method for the addition of co-catalysts on promising photoanodes for solar fuels and chemical production.

2. Results and Discussion

2.1. Structural and Morphological Analysis

Ti-Fe_2O_3 was chosen as a candidate to investigate the effects of CN and a supported catalyst. The fabrication process of the Ti-Fe_2O_3/CN/NCP photoanode is outlined in **Figure 1a**, with detailed information available in the Experimental Section of the Supporting Information. Initially, CN was obtained by annealing urea, followed by the growth of Ni-doped Co_3O_4 on CN (CN/NCO), and a subsequent phosphidization step to convert the CN-supported NCO to Ni-doped CoP (CN/NCP). Ni-doped CoP was chosen over CoP due to its superior performance.[33,34] Ti-doped Fe_2O_3 (Ti-Fe_2O_3) was hydrothermally synthesized on fluorine-doped tin oxide (FTO) coated glass. Finally, the Ti-Fe_2O_3/CN/NCP samples were obtained by spin-coating CN/NCP onto Ti-Fe_2O_3 six times. The morphology and thickness of the synthesized films were characterized by scanning electron microscopy (SEM). The SEM micrographs of Ti-Fe_2O_3 show that this is a porous and rough film of ≈2.5 µm thickness (Figure 1b,c). The added CN/NCP can be clearly observed in the SEM micrographs of Ti-Fe_2O_3/CN/NCP as dispersed graphitic material covering the rough and porous Ti-Fe_2O_3 (Figure 1d,e). No differences can be observed between the SEM micrographs of Ti-Fe_2O_3/CN/NCP and Ti-Fe_2O_3/CN, suggesting that NCP is of very small dimensions (Figure S1, Supporting Information). Transmission electron microscopy (TEM) micrographs of CN/NCP show that NCP nanoparticles are ≈10 nm wide and are well dispersed and embedded in the CN nanosheets (Figure S2, Supporting Information). TEM and high-resolution TEM (HRTEM) micrographs show that the Ti-Fe_2O_3 film consists of ≈100 nm nanoparticles. Their resolved lattice fringe with an interplanar spacing of 2.51 Å matches well with the (110) plane of α-Fe_2O_3 (Figure 1f,g; Figure S3, Supporting Information). TEM and HRTEM micrographs also show that surrounding the α-Fe_2O_3 particles, there are 10 nm CoP nanoparticles, with an interplanar spacing of 2.81 Å, corresponding to the (011) plane of CoP, embedded and uniformly dispersed in the CN sheets (Figure 1h,i; Figure S3, Supporting Information).[35] Energy dispersive X-ray spectroscopy (EDX) and TEM mapping (Figure S3d-l, Supporting Information) confirmed the existence of Fe, Ti, O, C, N, Ni, Co, and P elements, in which Fe, Ti, and O compose Ti-Fe_2O_3, C and N compose CN, and Ni, Co and P compose NCP. The EDX results demonstrate the homogeneous distribution of CN/NCP on the Ti-Fe_2O_3 film. To verify the crystal structure and phases of

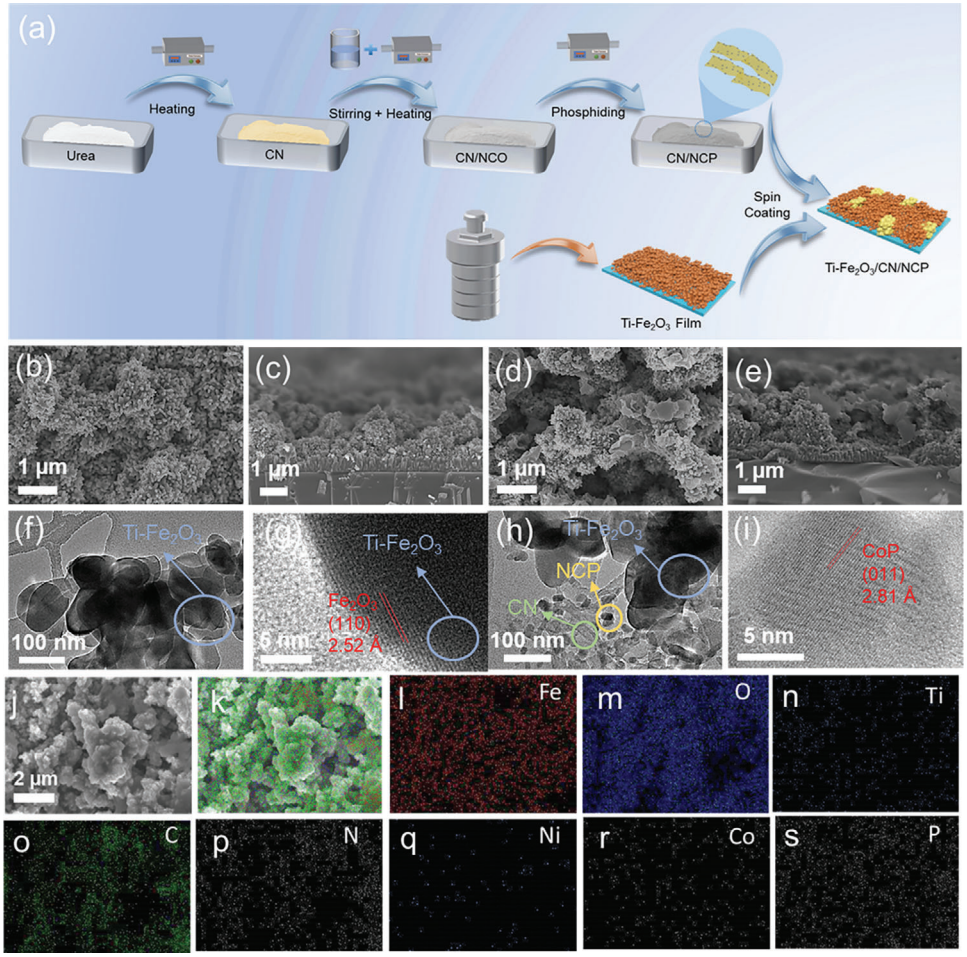

Figure 1. a) Schematic illustration of the synthesis of Ti-Fe_2O_3/CN/NCP. b,d) Top and c,e) cross-section SEM micrographs of b,c) Ti-Fe_2O_3 and d,e) Ti-Fe_2O_3/CN/NCP. f,h) TEM and g,i) HRTEM micrographs of f,g) Ti-Fe_2O_3 and h,i) Ti-Fe_2O_3/CN/NCP. j) SEM micrographs of Ti-Fe_2O_3/CN/NCP. k–s) EDX elemental maps of k) the overlap of all elements, l) Fe, m) O, n) Ti, o) C, p) N, q) Ni, r) Co, and s) P in Ti-Fe_2O_3/CN/NCP.

synthesized samples, X-ray diffraction (XRD) patterns were collected on the different materials (Figure S4a, Supporting Information). All the Ti-Fe_2O_3 samples produced well-defined diffraction peaks, characteristics of α-Fe_2O_3 (JCPDS 79-0007), while there are no obvious peaks for the loaded CN/NCP on the Ti-Fe_2O_3 samples due to its small dimensions and relatively smaller amount. The g-C_3N_4 XRD peaks can instead be observed in the CN, CN/NCO, and CN/NCP powder samples (Figure S4b, Supporting Information).[36] CN/NCO also shows another two peaks at 36.7 and 44.8° (2θ), corresponding to Co_3O_4 (JCPDS 29–0497), and CN/NCP shows instead two peaks at 31.7 and 48.2° (2θ), corresponding to CoP (JCPDS 42–1467).

To characterize the elemental composition of the surface and electronic states of the elements of the various components of the fabricated photoanodes, X-ray photoelectron spectroscopy (XPS) was carried out. The XPS survey spectrum of Ti-Fe_2O_3/CN/NCP shows that Fe, Ti, Co, Ni, C, N, and O elements exist in the composite photoanodes (Figure S5, Supporting Information), confirming the EDX data. High-resolution Fe *2p* XPS spectrum shows two intense peaks at 724.7 and 711.3 eV, corresponding to Fe $2p_{1/2}$ and Fe $2p_{3/2}$ in Fe_2O_3 (Figure S6a, Supporting Information).[37] High-resolution Ti *2p* XPS spectrum shows that the Ti doping on hematite exists in the form of Ti^{4+} (Figure S6b, Supporting Information).[38] High-resolution O *1s* XPS spectra exhibit three peaks located at 529.8, 531.0, and 532.5 eV, corresponding to metal (Fe, Co)—O, Fe—OH, and C—O bonds, respectively (**Figure 2a**). Combined with the analysis of XRD and TEM, the results confirm that the phase of Ti-Fe_2O_3 is pure α–Fe_2O_3, in which Ti is just a dopant that does not create a separate crystal phase. As displayed in Figure 2b, in pristine Ti-Fe_2O_3, the high-resolution C *1s* XPS spectra of Ti-Fe_2O_3 can be deconvoluted into two peaks at 284.8 and 286.1 eV, respectively, assigned to C—C bonds and C—O bonds, respectively,[39] whereas in Ti-Fe_2O_3/CN and Ti-Fe_2O_3/CN/NCP, there is an additional peak at 288.4 eV, which is assigned to N—C≡N bonds in CN. The presence of CN in Ti-Fe_2O_3/CN/NCP is further confirmed by the results in the high-resolution N *1s* XPS spectra in Figure 2c, in which the N *1s* spectrum exhibits two peaks at 406.1 and 398.4 eV, attributed to N—O and graphitic N, respectively, showing the successful synthesis and loading of g-C_3N_4 (Figure 2c).[40] Owing to the binding energy overlap of Co *2p* and Fe LMM, as well as the small amount loading of Co and Ni on composites to avoid

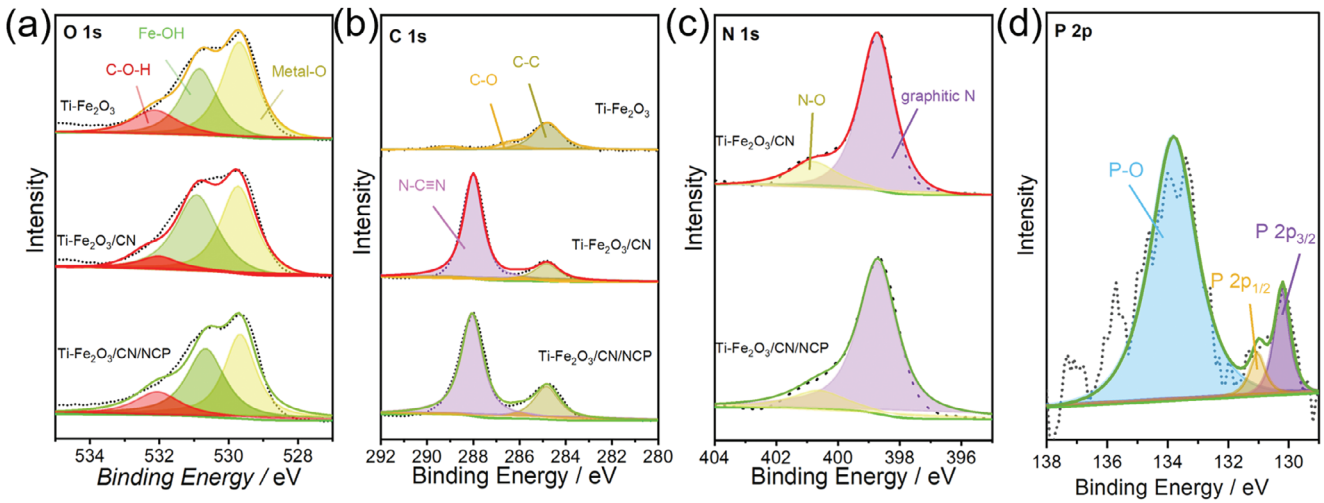

Figure 2. High-resolution XPS spectra of a) O 1s, b) C 1s, c) N 1s, and d) P 2p on the $Ti\text{-}Fe_2O_3$, $Ti\text{-}Fe_2O_3$/CN, and $Ti\text{-}Fe_2O_3$/CN/NCP photoanodes.

parasitic absorption and dark current,[41,42] the high-resolution XPS spectra of Co *2p* and Ni *2p* on $Ti\text{-}Fe_2O_3$, $Ti\text{-}Fe_2O_3$/CN, and $Ti\text{-}Fe_2O_3$/CN/NCP are not informative (Figure S6c,d, Supporting Information). Therefore, the high-resolution XPS spectra of Co 2p and Ni 2p of CN, CN/NCO, and CN/NCP were instead measured, confirming the existence of Co^{3+}/Co^{2+} and Ni^{3+}/Ni^{2+}, in agreement with literature.[43] In the high-resolution P *2p* XPS spectra in Figure 2d, three deconvoluted peaks can be observed with two peaks at 129.3 and 130.3 eV for P $2p_{3/2}$ and P $2p_{1/2}$, respectively, assigned to the core of the Ni-CoP nanoparticles, and one peak at a higher binding energy of ≈134 eV assigned to P—O bonds in P species like PO_4^{3-} or P_2O_5 due to surface oxidation.[44] These analyses confirm the successful synthesis and integration of CN and NCP with $Ti\text{-}Fe_2O_3$, highlighting the composite's complex structural and electronic characteristics essential for enhanced PEC performance.

2.2. PEC Water Oxidation

To evaluate the performance of the fabricated photoanodes, systematic photoelectrochemical (PEC) measurements were conducted in a three-electrode cell. Initially, the light-chopped current-potential (*j-V*) curves were measured in 1 M NaOH solution (pH 13.7) under simulated sunlight (100 mW cm^{-2}, AM 1.5 G) through the glass side (back illumination) (**Figure 3a**). All the photoanodes show a photoresponse upon turning on the light. The $Ti\text{-}Fe_2O_3$ photoanode shows a late onset potential at +0.8 V_{RHE}, in good agreement with most reported values for hematite due to Fermi level pinning at surface states that limit band bending for charge separation and injection to the electrolyte, as well as due to poor catalytic surface for the difficult 4-electron oxygen evolution reaction (OER).[45,46] The onset potential of $Ti\text{-}Fe_2O_3$ after coating with CN is slightly cathodically shifted to +0.75 V_{RHE} compared with $Ti\text{-}Fe_2O_3$ (+0.80 V_{RHE}), while the onset potential of $Ti\text{-}Fe_2O_3$ after coating with CN/NCP is clearly cathodically shifted to +0.60 V_{RHE}. In addition, $Ti\text{-}Fe_2O_3$/CN and $Ti\text{-}Fe_2O_3$/CN/NCP show enhanced photocurrents compared with pristine $Ti\text{-}Fe_2O_3$. Especially, $Ti\text{-}Fe_2O_3$/CN/NCP has a photocurrent of 2.01 mA cm^{-2} at +1.23 V_{RHE}, which is about 7 times higher than that of $Ti\text{-}Fe_2O_3$ (0.28 mA cm^{-2}). Comparison to other hematite/co-catalyst systems shows the relevance of this enhancement (Table S1, Supporting Information). Furthermore, to explore the function of CN, nickel-doped cobalt phosphides were synthesized with the same CoP phase (JCPDS 29–0479), as shown in the XRD pattern in Figure S7a (Supporting Information), and then spin-coated on $Ti\text{-}Fe_2O_3$ photoanode, resulting in $Ti\text{-}Fe_2O_3$/NCP photoanodes without CN. The PEC performance of $Ti\text{-}Fe_2O_3$/NCP is inferior to that of $Ti\text{-}Fe_2O_3$/CN/NCP (0.62 mA cm^{-2} versus 2.01 mA cm^{-2} at +1.23 V_{RHE}) and presents a large dark current, showing that the CN substrate is very important for the $Ti\text{-}Fe_2O_3$ photoanode assembly to achieve optimal PEC performance (Figure 3a). The NCP particle sizes grown outside the CN matrix were 163 nm average (Figure S7b,c, Supporting Information), compared with 10 nm in the CN matrix (Figure S2a,b, Supporting Information). Thus, we attribute the lower performance of $Ti\text{-}Fe_2O_3$/NCP in part to its larger NCP electrocatalyst particle dimensions, which provide less area for OER compared to 10-nm NCP particles on CN and must hamper effective charge transfer. Optimization studies confirm optimal amounts of Ti doping and CN/NCP (Figure S8a,c, Supporting Information), and statistical analysis shows good reproducibility and small standard deviation (Figure S9, Supporting Information). Further attention to the *j–V* curves under chopped light in the applied bias range from +0.6 to +1.1 V_{RHE} (Figure 3a, inset) shows positive spikes upon light illumination, suggesting hole accumulation in the space charge region, allowing the electron-hole separation and extraction of electrons to the external circuit.[47] This apparent accumulation increases in the order of $Ti\text{-}Fe_2O_3$ < $Ti\text{-}Fe_2O_3$/CN < $Ti\text{-}Fe_2O_3$/NCP < $Ti\text{-}Fe_2O_3$/CN/NCP (Figure 3a).[47]. This trend indicates that both CN and NCP show ability to accumulate charge carriers. Surface charge separation efficiencies were calculated by dividing the photocurrent densities without and with H_2O_2 hole scavenger (Figure S10a, Supporting Information).[4,48] $Ti\text{-}Fe_2O_3$/CN/NCP shows the highest efficiencies across the wide bias range, achieving a plateau of 69% beyond +1.35 V_{RHE}. Bulk charge separation efficiencies were calculated by dividing

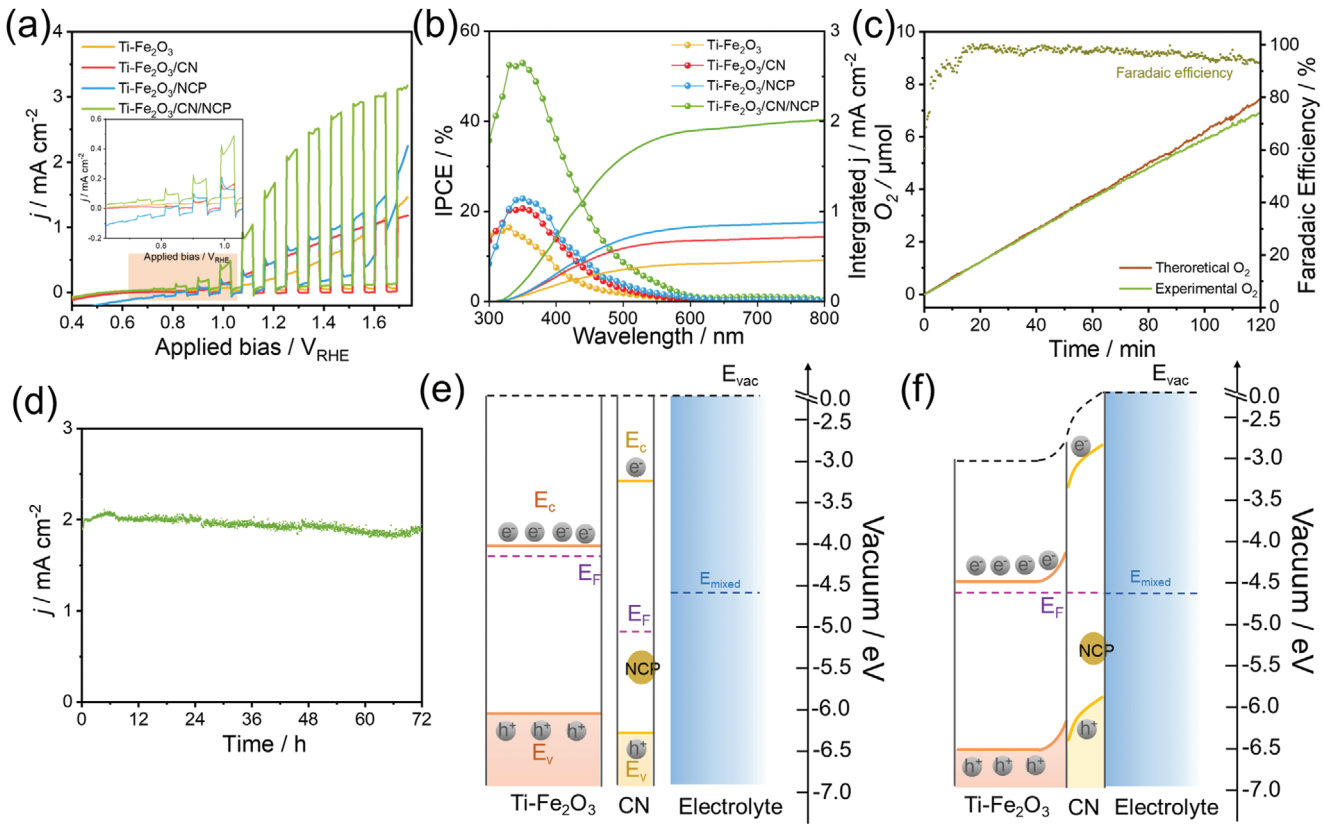

Figure 3. a) (Photo)current-potential curves of Ti-Fe_2O_3, Ti-Fe_2O_3/CN, Ti-Fe_2O_3/NCP, and Ti-Fe_2O_3/CN/NCP photoanodes under 1 sun (Xe source, AM 1.5G filter, 100 mW cm^{-2}) chopped illumination at a scan rate of 10 mV s^{-1}. Inset: zoomed in curves of (a) showing photocurrent onsets from +0.6 to +1.0 V_{RHE}. b) IPCE spectra at +1.23 V_{RHE} under monochromatic light (Xe source and monochromator) and integrated photocurrents of Ti-Fe_2O_3, Ti-Fe_2O_3/CN, Ti-Fe_2O_3/NCP, and Ti-Fe_2O_3/CN/NCP. c) Amount of measured and theoretical oxygen, and the calculated Faradaic efficiency of Ti-Fe_2O_3/CN/NCP at an applied bias of +1.23 V_{RHE}. d) Photocurrent stability test of Ti-Fe_2O_3/CN/NCP photoanode at +1.23 V_{RHE}. All these measurements were carried out in 1 M aqueous NaOH solution. e) Schematic band structure of Ti-Fe_2O_3/CN/NCP photoanode before contact. Note: E_{mixed} is electrode potential established from the interplay of different electrochemical processes at the electrode/electrolyte interphase (e.g., surface oxidations and reductions and OER).[49] f) Schematic band structure of Ti-Fe_2O_3/CN/NCP photoanode after contact.

photocurrent densities with H_2O_2 hole scavenger by those calculated assuming 100% absorbed photon-to-current conversion (Figure S10b,c, Supporting Information).[48] Ti-Fe_2O_3/CN/NCP achieves the highest bulk separation efficiency values at applied biases.

To identify the origin of the boosted photocurrent on Ti-Fe_2O_3/CN/NCP compared with Ti-Fe_2O_3, different photoanodes were prepared with different components. First, we prepared and measured the PEC performance of photoanodes with CN, CN/NCO, and CN/NCP without Ti-Fe_2O_3. The *j-V* curves in Figure S11a (Supporting Information) indicate that CN, CN/NCO, and CN/NCP films show no photoresponse, meaning that the produced photocurrent in Ti-Fe_2O_3/CN/NCP (Figure 3a) comes exclusively from photo-induced charges in Ti-Fe_2O_3 rather than those of the topping layers. In addition, to exclude the influence of the phosphidization process on CN, the PEC performance of phosphidized CN (CNP) on Ti-Fe_2O_3 (Ti-Fe_2O_3/CNP), following the same preparation procedure, was also measured and found to be the same as Ti-Fe_2O_3/CN (Figure S11b, Supporting Information), so any phosphorus addition to CN has no apparent influence on photocurrents. To confirm the advantage of phosphiding the NCO (Ni-Co_3O_4) particles to NCP (Ni-CoP) for PEC performance, the *j-V* curves of Ti-Fe_2O_3/CN/NCO were also measured, showing a lower photocurrent of 1.33 mA cm^{-2} at +1.23 V_{RHE} compared with the 2.01 mA cm^{-2} of Ti-Fe_2O_3/CN/NCP (Figure S12, Supporting Information). Altogether, the high PEC photocurrent of Ti-Fe_2O_3/CN/NCP compared with the other studied photoanodes demonstrates a synergistic effect achieved by the integration of both CN and NCP on Ti-Fe_2O_3.

The incident photon-to-current efficiency (IPCE) spectra of Ti-Fe_2O_3, Ti-Fe_2O_3/CN, Ti-Fe_2O_3/NCP, and Ti-Fe_2O_3/CN/NCP were measured at +1.23 V_{RHE} to further understand the PEC performance of each photoanode (Figure 3b). Ti-Fe_2O_3/CN/NCP shows significantly enhanced IPCE values compared with Ti-Fe_2O_3, reaching 52.9% at 350 nm, trippling that of Ti-Fe_2O_3 (16.4%). The IPCE curves of the three photoanodes show the same trend and onset, indicating that the improved photocurrents are not due to extra wavelength absorbed with the addition of the topping layers, but due to better light utilization in the same spectrum range. The integration of the IPCE curves with respect to the solar spectrum was done and shown to achieve similar photocurrents to those under the simulated sunlight (Figure 3a,b). To verify that the photocurrents are due to

solar-driven OER, we measured the oxygen evolution with a fluorescence probe with Ti-Fe_2O_3/CN/NCP, at +1.23 V_{RHE} in 1 M NaOH for 2 h (Figure 3c). The calculated Faradaic efficiency was ≈100% during the first hour and just decreased to 95% in the second hour probably due to oxygen reduction in the counter electrode or leakage upon built-up pressure. The Faradaic results indicate that the increased photocurrent comes from OER rather than any photoanode material oxidation. Moreover, the PEC performance of Ti-Fe_2O_3/CN/NCP at +1.23 V_{RHE} was shown to be stable for 72 h, since no obvious decay in photocurrent density was observed (Figure 3d).

2.3. Energetics

To understand the enhanced PEC performance for water oxidation reaction, the ultraviolet-visible absorptance spectra of the photoanodes with back illumination (through the glass side) and front illumination (through the material side) using a diffuse reflectance sphere (DRS) were explored first. The DRS spectra under back illumination show that the introduction of CN and CN/NCP increases the absorptance below 600 nm attributed to the Ti-Fe_2O_3 band gap (Figure S13a, Supporting Information). However, under front illumination, the absorptance decreases with the use of CN and CN/CNP (Figure S13b, Supporting Information). These differences in the two spectra indicate that CN acts partly as a reflective coating, increasing the chances for light to be absorbed in the Ti-Fe_2O_3. The substantial decrease of absorptance on Ti-Fe_2O_3/CN compared with Ti-Fe_2O_3/CN/CNP in Figure S13b (Supporting Information) is due to the larger volume of CN in the former. The same weight was spin-coated in both cases, but CN is less dense than CN/CNP resulting in more coverage (and then more reflective effect). Next, we measured and constructed the energy band diagrams of the materials using the information obtained via UV-vis spectroscopy, Kelvin probe, and APS. The CN exhibits strong absorption in the UV region with an absorption edge at ≈400 nm and a calculated indirect band gap of 2.8 eV using a Tauc plot (Figure S14a,b, Supporting Information). Ti-Fe_2O_3 exhibits strong absorption in the visible region with an absorption edge at ≈575 nm and a calculated direct band gap of 2.1 eV (Figure S14c,d, Supporting Information). APS was used to investigate the valence band of CN and Ti-Fe_2O_3, which were located at −6.2 and −6.0 eV from vacuum level, respectively (Figure S15a, Supporting Information). The Kelvin probe located the Fermi level of the Ti-Fe_2O_3 film at ≈ −4.1 eV and that of the CN film at ≈ −5.8 eV from vacuum level (Figure S15b, Supporting Information). With this information, the energy band diagram of the components of the Ti-Fe_2O_3/CN/NCP photoanode before contact was constructed and illustrated in Figure 3f. The energy diagram shows that CN has a deeper Fermi level than Ti-Fe_2O_3, so the equilibration of their Fermi levels upon contact will induce strong downward band bending in the CN interface side and upward band bending in the Ti-Fe_2O_3 interface side as illustrated in Figure 3g. The energy diagram of this heterostructure indicates that they form a type-II heterojunction, which forms a built-in electric field at the interface that boosts charge separation and explains in part the observed enhanced photocurrents in Figure 3a.

Open circuit potential (OCP) measurements were conducted under 1 sun irradiation and in dark conditions (Figure S16a, Supporting Information). The OCPs under 1 sun were +0.67 V_{RHE} for Ti-Fe_2O_3/CN/NCP and +0.71–0.72 V_{RHE} for the rest of samples, in agreement with the more cathodic onset potential observed on Ti-Fe_2O_3/CN/NCP in Figure 3a. Upon switching off the light, the OCP in the dark equilibrated at ≈ +0.8 V_{RHE}, far from the water oxidation potential of +1.23 V_{RHE}, indicating a more complex electrode/electrolyte interface where different electrochemical processes interplay (e.g., surface oxidations and reductions and OER) resulting in a mixed potential (E_{mixed}).[49] The differences in OCP between illumination and dark conditions indicate a higher photovoltage in Ti-Fe_2O_3/CN/NCP, also in agreement with the more cathodic onset potential. Furthermore, a faster OCP increase upon switching off the light is observed on the samples containing CN. These OCP transients were used to calculate OCP-derived charge carrier lifetimes (τ_n) following previously published methods (Figure S16b, Supporting Information).[8,50,51] Shorter τ_n have been suggested to be indicative of more efficient charge separation under illumination. The calculated τ_n values were 885 ms in Ti-Fe_2O_3 and a significantly shorter 301 and 167 ms in Ti-Fe_2O_3/CN and Ti-Fe_2O_3/CN/NCP, respectively. These indicate much more efficient charge separation and rapid transfer kinetics in the Ti-Fe_2O_3/CN and Ti-Fe_2O_3/CN/NCP, attributed to the type-II heterojunction between Ti-Fe_2O_3 and CN and further boosted with the added NCP functionality.

2.4. OER Kinetics

IMPS was carried out to delve deeper into the kinetics of the photoanodes. IMPS involves applying a small modulation to the light intensity incident on a photoelectrode and measuring the resultant changes in photocurrent as a function of modulation frequency. Since IMPS does not directly measure hole dynamics, it relies on a theoretical framework to deduce kinetic parameters. Typically, the IMPS plots of hematite photoanodes exhibit two semicircles, one at high frequency (HF) in the fourth quadrant and another at low frequency (LF) in the first quadrant, as shown in **Figures** 4a–c and S17 (Supporting Information).[52,53] At low applied bias, such as +0.85 V_{RHE} (near the flat band potential of these photoanodes), the left intersections of the LF semicircle and X-axis of all the photoanodes are near the origin, suggesting that most surface holes recombine (Figure 4a). With the increasing bias, smaller LF semicircles and larger HF semicircles are observed, indicating reduced recombination of holes and increased hole flux to the surface of photoanodes, respectively.[54] When the applied bias is high enough to suppress the charge recombination, for example, +1.25 V_{RHE}, Ti-Fe_2O_3/CN/NCP does not show an LF semicircle, indicating almost no surface recombination, something that is not achieved with the other photoanodes (Figure 4c). Compared with Ti-Fe_2O_3 and Ti-Fe_2O_3/CN, Ti-Fe_2O_3/CN/NCP possesses the largest HF semicircle, that is the largest hole flux, at +1.25 V_{RHE}, consistent with previous results of photocurrents in Figure 3.

The rate constants of charge transfer (k_{ct}) and surface recombination (k_{rec}) on the IMPS plots can be calculated using a phenomenological model developed by Peter et al.[52,55] The

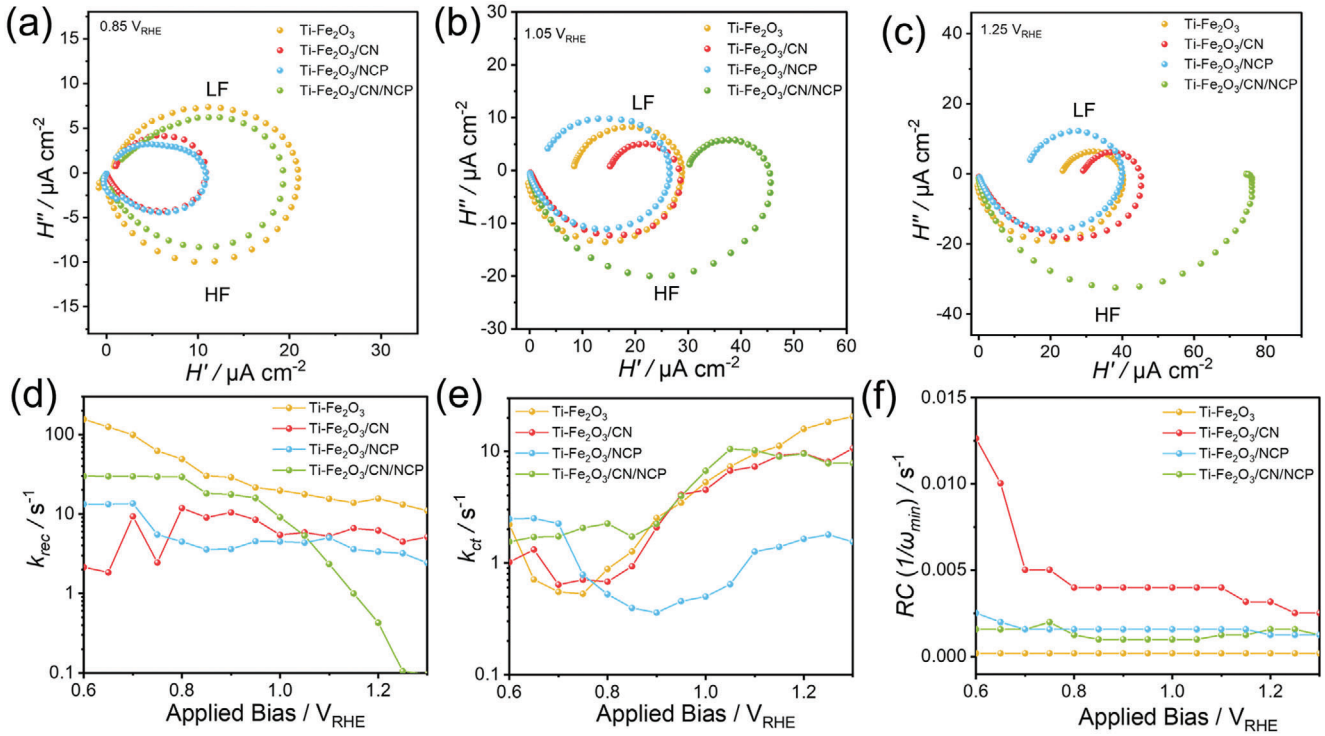

Figure 4. a–c) IMPS plots of Ti-Fe_2O_3, Ti-Fe_2O_3/CN, Ti-Fe_2O_3/NCP, and Ti-Fe_2O_3/CN/NCP photoanodes as a function of applied bias at +0.85, +1.05, and +1.25 V_{RHE} in 1 M NaOH solution under 455 nm LED illumination (37.5 mW cm^{-2}) with modulation of 50% in light intensity, over a frequency range from 10 [3] to 0.1 Hz at each potential step. c,d) rate constants (k_{rec} and k_{ct}) and time constant RC calculated using IMPS plots at various potentials.

calculated k_{rec} values at different biases are significantly lower in CN-containing photoanodes, indicating reduced surface ('back electron-hole') recombination (Figure 4d).[56] We attribute these lower k_{rec} values to the formed type-II heterojunction with the addition of CN on Ti-Fe_2O_3 surfaces. Calculated charge-transfer kinetic constant (k_{ct}) values show similar results on Ti-Fe_2O_3 and Ti-Fe_2O_3/CN, but boosted k_{ct} on Ti-Fe_2O_3/CN/NCP at low applied bias values ≈ +0.8 V_{RHE} (Figure 4e), in agreement again with the improved onset potential for photocurrents and OCP values under light. We attribute these enhanced charge transfer kinetics to the NCP catalyst presence and activity.[41] Calculated time constants (τ) show higher values on photoanodes with loaded CN and CN/NCP, particularly on Ti-Fe_2O_3/CN (Figure 4f). The increased τ values suggest that the loading of CN leads to a longer lifetime of photogenerated holes, but this effect is reduced with the addition of NCP due to desirable migration and surface reaction with the catalytically active fine NCP nanoparticles.[57] The kinetic results are consistent with the schematic energy model proposed for hole transfer routes in Figure 3g and a type-II heterojunction. The CN coating layer not only passivates surface states on Ti-Fe_2O_3 and forms a type-II heterojunction with Ti-Fe_2O_3 lowering recombination but also increases the lifetime of photoinduced holes, while fine NCP particles boost charge transfer to the electrolyte and OER.

TAS measurements directly probe populations and lifetimes of photoinduced charge carriers in the photoactive layer and thus give insight into charge carrier dynamics complementary to the IMPS measurements discussed thus far, which probe the kinetics of electrons extracted to the external circuit. Bias-dependent TAS measurements at 650 nm, previously assigned to Fe_2O_3 valence band holes,[58] were carried out to investigate the impact of CN and NCP on hole dynamics in Ti-Fe_2O_3 (**Figure 5**). Under open circuit potential (OCP), the TAS decay kinetics, assigned to electron/hole recombination, are similar for all four samples. There is a higher initial hole signal in Ti-Fe_2O_3/CN/NCP compared to Ti-Fe_2O_3 alone, suggesting some space charge layer formation in the junction material. However, this difference in amplitude, without an associated change in decay kinetics, is not sufficient to explain the improvement in PEC performance. It is, for example, significantly less than that observed previously for Fe_2O_3/Co-Pi [25] or Fe_2O_3/CoO_x [59] photoanodes.

With increasing anodic bias, the initial hole population increases for all four films, as expected for increased band bending and in line with TAS studies across a range of metal oxides.[59,60] Under strong anodic bias (e.g., 1.60 V_{RHE}, Figure 5; Figure S18c, Supporting Information), deposition of CN, NCP, or CN/NCP on Ti-Fe_2O_3 results in an increase in hole population on the μs-ms timescale (Figure 5b–d) compared to Ti-Fe_2O_3 alone. This indicates these layers result in suppressed recombination losses, in agreement with the k_{rec} values calculated from the IMPS plots, discussed above (Figure 4d). The increase in hole population is largest for Ti-Fe_2O_3/CN, which also demonstrates the most pronounced bias dependence and has the highest initial hole signal (Figure 5b). It is striking that, despite having the highest initial hole signal, the transient hole signal for Ti-Fe_2O_3/CN under 1.6 V_{RHE} decays faster than for the other films, going to ≈ zero by 10 ms (faster than the timescale of OER).

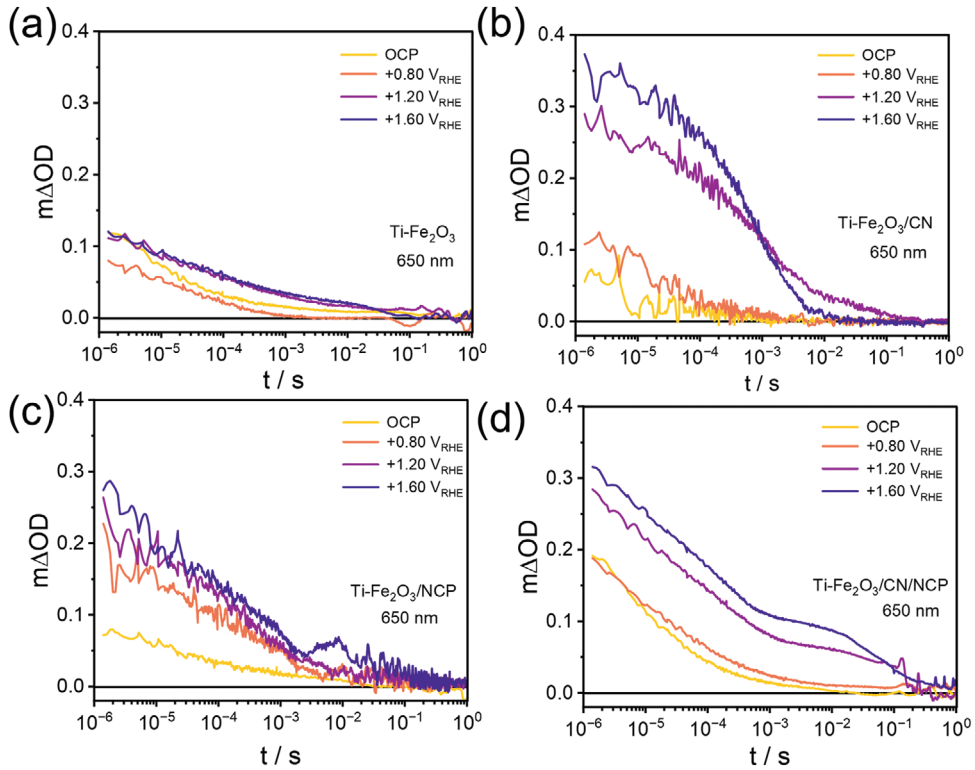

Figure 5. Transient absorption decays of a) Ti-Fe_2O_3, b) Ti-Fe_2O_3/CN, c) Ti-Fe_2O_3/NCP, and d) Ti-Fe_2O_3/CN/NCP films under open circuit potential, 0.8, 1.2, and 1.6 V_{RHE}. Decay traces probed at 650 nm after laser excitation at 355 nm (≈200 μJ cm^{-2}, 1 Hz).

This rapid hematite hole signal decay suggests the holes are transferred from the Ti-Fe_2O_3 to the CN; holes in CN exhibit negligible visible light absorption.[61] Furthermore, there is only a small increase in photocurrent performance after the addition of CN to Ti-Fe_2O_3 (Figure 3a), suggesting the holes in CN are not particularly active for OER. This is consistent with previous studies.[62,63]

In contrast to Ti-Fe_2O_3/CN, the 650 nm hole signal in Ti-Fe_2O_3/CN/NCP under 1.60 V_{RHE} exhibits an additional, much slower (100 ms half time) decay phase (Figure 5d; Figure S18c, Supporting Information). Whilst some contribution to this slow decay phase from long-lived Ti-Fe_2O_3 holes cannot be ruled out, the appearance of this slow decay phase with NCP addition suggests it originates from the holes that transfer from the CN to the NCP. Previous work on a similar co-catalyst material, Co-Pi, found its holes showed a broad absorption feature from 500–900 nm.[64] It is therefore likely that at later timescales, the 650 nm absorption signal in Ti-Fe_2O_3/CN/NCP is dominated by holes in the NCP.

The decay kinetics of Ti-Fe_2O_3/NCP (Figure 5c) show a very similar shape and bias dependence to Ti-Fe_2O_3 but larger hole signals, indicative of improved charge separation. The hole signal at later timescales is smaller than that for Ti-Fe_2O_3/CN/NCP, indicative of the key role of CN in mediating hole transfer from the Ti-Fe_2O_3 to the NCP. Ti-Fe_2O_3/CN/NCP exhibits a significantly higher hole signal at OER timescales compared to all other samples. Moreover, it presents a clearer two-phase decay at higher applied biases, indicating an abundance of holes in the system during the OER process, in agreement with its photocurrent response (Figure 3a) and IMPS response (Figure 4).

TAS measurements were also carried out at 580 nm for Ti-Fe_2O_3 and Ti-Fe_2O_3/CN/NCP (**Figure 6**) to probe a bleach signal previously observed and assigned to photogenerated electrons.[59] More specifically, this bleach signal is assigned to electrons trapped in Fe_2O_3 defect states in the SCL (most likely oxygen vacancies), that subsequently undergo thermally activated detrapping and extraction to the external circuit resulting in photocurrent generation.[59] For both films, this bleach signal increases in magnitude with increasing anodic bias, indicating more electron trapping. This result correlates well with the increasing magnitude of the positive 650 nm hole signal with increasing anodic bias, and provides further confirmation of increased charge separation, due to bias-induced increased band bending resulting in higher populations of both electrons and holes. For Ti-Fe_2O_3/CN/NCP the negative 580 nm and positive 650 nm signals are both larger than for Ti-Fe_2O_3 alone. This shows that the larger hole signals in Ti-Fe_2O_3/CN/NCP are correlated with larger electron signals. This is consistent with improved charge separation compared to Ti-Fe_2O_3 alone, which significantly improved photocurrent performance for Ti-Fe_2O_3/CN/NCP compared to Ti-Fe_2O_3 (Figure 3a) and IMPS data as discussed previously. This bleach signal only appears under anodic applied biases and is not present at OCP, in agreement with the 650 nm OCP data, and it suggests only minimal space charge layer formation in the Ti-Fe_2O_3/CN/NCP film at OCP.

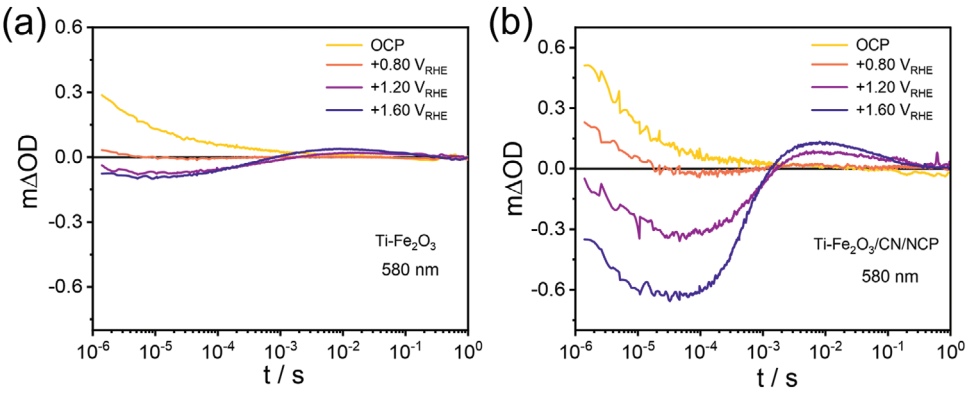

Figure 6. Transient absorption decays of a) Ti-Fe_2O_3 and b) Ti-Fe_2O_3/CN/NCP films under open circuit potential, 0.80, 1.20 and 1.60 V_{RHE}. Decay traces probed at 580 nm after laser excitation at 355 nm (≈200 μJ cm^{-2}, 1 Hz).

2.5. Discussion

Based on the TAS characterization and subsequent analysis, different routes for hole transfer and OER reactions on Ti-Fe_2O_3-based photoanodes are proposed as shown in **Figure 7**. For pristine Ti-Fe_2O_3 photoanodes, the photogenerated holes are transferred to the surface of Ti-Fe_2O_3 driven by the upward band bending in the space charge region and the anodic applied bias for the OER reaction to occur (Figure 7a). With a CN coating on Ti-Fe_2O_3, the type-II heterojunction formed generates a built-in electric field that increases charge separation and hole surface population. While CN does not have OER catalytic activity, OER can still happen on the surface of Ti-Fe_2O_3 with slightly boosted photocurrents (Figure 7b). Coating Ti-Fe_2O_3 with NCP, in the absence of CN, extends the lifetime of transferred holes from Ti-Fe_2O_3 to NCP catalyst, permitting further OER reaction and enhanced photocurrents (Figure 7c). The integration of CN and CN-supported finer NCP on Ti-Fe_2O_3 combines both CN and NCP benefits and synergistically reaches enhanced OER and photocurrents. The photogenerated holes in Ti-Fe_2O_3/CN/NCP are first transferred from Ti-Fe_2O_3 to CN via the formed type-II heterojunction, then further transferred to the fine NCP catalyst for the most enhanced OER reaction and highest photocurrent (Figure 7d). Some degree of direct hole transfer from Ti-Fe_2O_3 to NCP also occurs.

The characterizations collectively and complementarily indicate that adding NCP electrocatalysts confined in a CN matrix on Ti-Fe_2O_3 photoanodes significantly boosts (by 7 times) solar OER photocurrents due to three main different factors that synergistically favor performance. First, CN acts as a reflective layer that enables enhanced light absorption by the hematite layer when illuminated through the glass side, as observed by UV-vis spectroscopy (Figure S13, Supporting Information). Second, the formation of a type-II heterojunction between Ti-Fe_2O_3 and CN in the photoanodes helps to separate photoinduced charges and reduce surface recombination, thereby boosting photon to current conversion efficiencies (Figures 3 and 4).[65–67] The CN presence is key to enhancing the charge separation, transfer and shuttling of photoinduced holes to the NCP catalyst that is more effective at driving OER than the Fe_2O_3 surface (Figures 5,6). CN/NCP is very effective at increasing both the hole population and their lifetime to the ms-s range needed for OER as both IMPS and TAS complementarily show (Figures 5–7). Third, growing the NCP electrocatalyst in the 2D graphitic CN matrix effectively restricts the electrocatalyst particle growth and aggregation, keeping their dimensions ≈10 nm compared with 163 nm if grown outside a

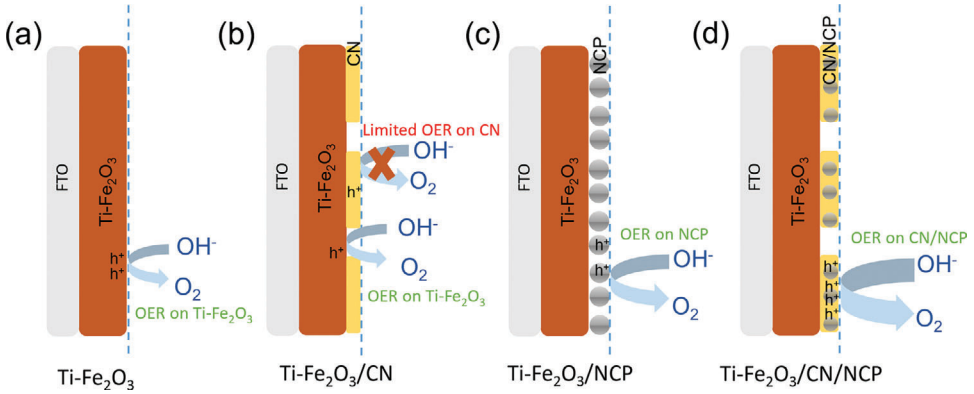

Figure 7. Schematic models for hole transfer routes and OER reactions on a) bare Ti-Fe_2O_3, b) Ti-Fe_2O_3/CN, c) Ti-Fe_2O_3/NCP, and d) Ti-Fe_2O_3/CN/NCP. Ti-Fe_2O_3 is represented in rust color, CN in yellow color, and NCP in grey dots of different sizes. The arrow width is proportional to the magnitude of the OER photocurrent.

matrix (Figures S2 and S7, Supporting Information). The smaller NCP size results in a larger electrocatalyst surface area, that is more active sites for OER, and probably a more effective contact with the Ti-Fe_2O_3 in direct charge transfers between both.[68,69] Collectively, these factors synergistically improve all the operational sequential steps of the Ti-Fe_2O_3-based photoanode, from the absorption of light to generate charges to their separation, transfer, and effective utilization to drive PEC OER from aqueous electrolytes.

3. Conclusion

This study demonstrates an effective strategy to enhance hematite photoanode performance by incorporating g-C_3N_4 nanosheets with anchored fine Ni-CoP nanoparticles. The optimized Ti-Fe_2O_3/g-C_3N_4/Ni-CoP photoanodes exhibit an enhanced photocurrent density (2.01 mA cm^{-2} at +1.23 V_{RHE}), 7 times higher than the same Ti-Fe_2O_3 alone (0.28 mA cm^{-2} at +1.23 V_{RHE}). Various spectroscopic techniques have underscored the critical role of efficiently interfacing the Ni-CoP cocatalyst with the hematite layer. The improvement in photocurrent with the g-C_3N_4/Ni-CoP layer is attributed to several synergistic factors: g-C_3N_4 enhances light absorption under back illumination by acting as a reflective coating, forms a type-II heterojunction with Ti-Fe_2O_3 boosting charge separation and hole transfer, and supports the growth of fine Ni-CoP nanoparticles for more effective catalysis. Additionally, g-C_3N_4 facilitates the accumulation and transfer of photoinduced holes to the Ni-CoP catalyst, extending their lifetime for the slow (ms-s) oxygen evolution reaction. These results not only unveil a novel application of g-C_3N_4 as a multifunctional support for fine cocatalysts but also present an effective strategy for interfacing high-performance electrocatalysts with semiconductor photoanodes, offering a significant advancement in photoelectrochemical systems.

Supporting Information

Supporting Information is available from the Wiley Online Library or from the author.

Acknowledgements

The authors thank the Department of Chemical Engineering at Imperial College London for the funding of a Ph.D. scholarship for M.Y. L.I.O. thanks Imperial College London's Faculty of Natural Sciences Schrödinger Scholarship for Ph.D. funding. S.E. and M.D. thank the UK EPSRC grant EP/S030727/1 for financial support. D.B. thanks the UK EPSRC grant EP/X027430/1 for financial support.

Conflict of Interest

The authors declare no conflict of interest.

Data Availability Statement

The data that support the findings of this study are openly available in a data repository at https://doi.org/10.6084/m9.figshare.25809745.

Keywords

hematite photoanodes, mechanism analysis, PEC water oxidation, ultrafine cocatalysts

Received: March 22, 2024
Revised: May 5, 2024
Published online: May 17, 2024

[1] K.-Y. Yoon, J. Park, H. Lee, J. H. Seo, M.-J. Kwak, J. H. Lee, J.-H. Jang, *ACS Catal.* **2022**, *12*, 5112.
[2] H. Han, S. Kment, F. Karlicky, L. Wang, A. Naldoni, P. Schmuki, R. Zboril, *Small.* **2018**, *14*, 1703860.
[3] J. Liu, Z. Luo, X. Mao, Y. Dong, L. Peng, D. Sun-Waterhouse, J. V. Kennedy, G. I. N. Waterhouse, *Small.* **2022**, *18*, 2204553.
[4] R.-T. Gao, N. T. Nguyen, T. Nakajima, J. He, X. Liu, X. Zhang, L. Wang, L. Wu, *Sci. Adv.* **2023**, *9*, eade4589.
[5] J. Deng, Y. Li, Y. Xiao, K. Feng, C. Lu, K. Nie, X. Lv, H. Xu, J. Zhong, *ACS Catal.* **2022**, *12*, 7833.
[6] C. Li, Z. Luo, T. Wang, J. S Gong, *Adv. Mater.* **2018**, *30*, 1707502.
[7] R.-T. Gao, J. Zhang, T. Nakajima, J. He, X. Liu, X. Zhang, L. Wang, L. Wu, *Nat. Commun.* **2023**, *14*, 2640.
[8] H. Zhang, D. Li, W. J. Byun, X. Wang, T. J. Shin, H. Y. Jeong, H. Han, C. Li, J. S. Lee, *Nat. Commun.* **2020**, *11*, 4622.
[9] T. H. Jeon, G. Moon, H. Park, W. Choi, *Nano Energy.* **2017**, *39*, 211.
[10] J. C. N. Fouemina, G. Li, X. She, D. Yan, X. Lv, K. Nie, J. Deng, H. Xu, *Small.* **2023**, *19*, 2301114.
[11] S. Shen, S. A. Lindley, X. Chen, J. Z. Zhang, *Energy Environ. Sci.* **2016**, *9*, 2744.
[12] R.-T. Gao, L. Liu, Y. Li, Y. Yang, J. He, X. Liu, X. Zhang, L. Wang, L. Wu, *Proc. Natl. Acad. Sci. USA.* **2023**, *120*, 2300493120.
[13] Š. Kment, K. Sivula, A. Naldoni, S. P. Sarmah, H. Kmentová, M. Kulkarni, Y. Rambabu, P. Schmuki, R. Zbořil, *Prog. Mater. Sci.* **2020**, *110*, 100632.
[14] Z. Li, W. Luo, M. Zhang, J. Feng, Z. Zou, *Energy Environ. Sci.* **2013**, *6*, 347.
[15] R. Zhang, L. Yang, X. Huang, T. Chen, F. Qu, Z. Liu, G. Du, A. M. Asiri, X. Sun, *J. Mater. Chem. A.* **2017**, *5*, 12086.
[16] J. Xie, P. Yang, X. Liang, J. Xiong, *ACS Appl. Energy Mater.* **2018**, *1*, 2769.
[17] C. Miao, T. Shi, G. Xu, S. Ji, C. Ye, *ACS Appl. Mater. Interfaces.* **2013**, *5*, 1310.
[18] Q. Yu, X. Meng, T. Wang, P. Li, J. Ye, *Adv. Funct. Mater.* **2015**, *25*, 2686.
[19] L. Wang, Y. Yang, Y. Zhang, Q. Rui, B. Zhang, Z. Shen, Y. Bi, *J. Mater. Chem. A.* **2017**, *5*, 17056.
[20] L. Mao, Yu-C Huang, H. Deng, F. Meng, Y. Fu, Y. Wang, M. Li, Q. Zhang, C-Li Dong, L. Gu, S. Shen, *Small.* **2023**, *19*, 2203838.
[21] B. Zhao, C. Feng, X. Huang, Y. Ding, Y. Bi, *J. Mater. Chem. A.* **2022**, *10*, 2813.
[22] P. S. Bassi, R. P. Antony, P. P. Boix, Y. Fang, J. Barber, L. H. Wong, *Nano Energy.* **2016**, *22*, 310.
[23] R. Subbaraman, D. Tripkovic, K.-C. Chang, D. Strmcnik, A. P. Paulikas, P. Hirunsit, M. Chan, J. Greeley, V. Stamenkovic, N. M. Markovic, *Nat. Mater.* **2012**, *11*, 550.
[24] J. Cai, S. Li, G. Qin, *Appl. Surf. Sci.* **2019**, *466*, 92.
[25] M. Barroso, A. J. Cowan, S. R. Pendlebury, M. Grätzel, D. R. Klug, J. R. Durrant, *J. Am. Chem. Soc.* **2011**, *133*, 14868.
[26] Y. Zhao, H. Shi, D. Yang, J. Fan, X. Hu, E. Liu, *J. Phys. Chem. C.* **2020**, *124*, 13771.
[27] N. Kumar, M. Mrinalini, S. Bastia, R. P. Mishra, M. K. Sahoo, Y. S. Chaudhary, *ChemCatChem.* **2023**, *15*, 202300266.
[28] M. Ismael, *J. Alloys Compd.* **2020**, *846*, 156446.

[29] X. Zou, Z. Sun, Y. H. Hu, *J. Mater. Chem. A.* **2020**, *8*, 21474.
[30] K.-H. Ye, H. Li, D. Huang, S. Xiao, W. Qiu, M. Li, Y. Hu, W. Mai, H. Ji, S. Yang, *Nat. Commun.* **2019**, *10*, 3687.
[31] H. Gao, H. Yang, J. Xu, S. Zhang, J. Li, *Small.* **2018**, *14*, 1801353.
[32] X. Zou, Y. Zhang, *Chem. Soc. Rev.* **2015**, *44*, 5148.
[33] J. Cui, M. Daboczi, Z. Cui, M. Gong, J. Flitcroft, J. Skelton, S. C. Parker, S. Eslava, *Small.* **2024**, *20*, 2306757.
[34] X. Sun, C. Liu, P. Zhang, L. Gong, M. Wang, *J. Power Sources.* **2021**, *484*, 229272.
[35] K. He, T. Tadesse Tsega, X. Liu, J. Zai, X.-H. Li, X. Liu, W. Li, N. Ali, X. Qian, *Angew. Chem., Int. Ed.* **2019**, *58*, 11903.
[36] F. Fina, S. K. Callear, G. M. Carins, J. T. S. Irvine, *Chemistry of Materials.* **2015**, *27*, 2612.
[37] L. Gao, H. Chai, H. Niu, J. Jin, J. Ma, *Small.* **2023**, *19*, 2302665.
[38] H. R. Devi, B. C. Ong, X. Zhao, Z. Dong, K. K. Nanda, Z. Chen, *Energy Technol.* **2022**, *10*, 2100457.
[39] Y. Meng, G. Wang, M. Xiao, C. Duan, C. Wang, F. Zhu, Y. Zhang, *J. Mater. Sci.* **2017**, *52*, 13192.
[40] Y. Li, S. Wu, L. Huang, J. Wang, H. Xu, H. Li, *Mater. Lett.* **2014**, *137*, 281.
[41] J. Zhang, R. García-Rodríguez, P. Cameron, S. Eslava, *Energy Environ. Sci.* **2018**, *11*, 2972.
[42] Y. B. Hu, C. F. Dong, M. Sun, K. Xiao, P. Zhong, X. G. Li, *Corros. Sci.* **2011**, *53*, 4159.
[43] Z. Ren, V. Botu, S. Wang, Y. Meng, W. Song, Y. Guo, R. Ramprasad, S. L. Suib, P.-X. Gao, *Angew. Chem. Int. Ed.* **2014**, *53*, 7223.
[44] J. Yu, Y. Zhong, X. Wu, J. Sunarso, M. Ni, W. Zhou, Z. Shao, *Adv. Sci.* **2018**, *5*, 1800514.
[45] Z. Fan, Z. Xu, S. Yan, Z. Zou, *J. Mater. Chem. A.* **2017**, *5*, 8402.
[46] J. Zhang, S. Eslava, *Sustainable Energy Fuels.* **2019**, *3*, 1351.
[47] G. Liu, S. Ye, P. Yan, F. Xiong, P. Fu, Z. Wang, Z. Chen, J. Shi, C. Li, *Energy Environ. Sci.* **2016**, *9*, 1327.
[48] M. Regue, I. Y. Ahmet, P. S. Bassi, A. L. Johnson, S. Fiechter, R. van de Krol, F. F. Abdi, S. Eslava, *ACS Appl. Energy Mater.* **2020**, *3*, 12066.
[49] G. P. Power, I. M. Ritchie, *J. Chem. Educ.* **1983**, *60*, 1022.
[50] A. Zaban, M. Greenshtein, J. Bisquert, *ChemPhysChem.* **2003**, *4*, 859.
[51] M. Zhong, T. Hisatomi, Y. Kuang, J. Zhao, M. Liu, A. Iwase, Q. Jia, H. Nishiyama, T. Minegishi, M. Nakabayashi, N. Shibata, R. Niishiro, C. Katayama, H. Shibano, M. Katayama, A. Kudo, T. Yamada, K. Domen, *J. Am. Chem. Soc.* **2015**, *137*, 5053.
[52] K. G. Upul Wijayantha, S. Saremi-Yarahmadi, L. M. Peter, *Phys. Chem. Chem. Phys.* **2011**, *13*, 5264.
[53] E. A. Ponomarev, L. M. Peter, *J. Electroanal. Chem.* **1995**, *396*, 219.
[54] C. Y. Cummings, F. Marken, L. M. Peter, A. A. Tahir, K. G. U. Wijayantha, *Chem. Commun.* **2012**, *48*, 2027.
[55] L. M. Peter, E. A. Ponomarev, D. J. Fermín, *J. Electroanal. Chem.* **1997**, *427*, 79.
[56] H.-J. Lewerenz, L. Peter *Photoelectrochemical Water Splitting: Materials, Processes and Architectures*, Royal Society of Chemistry, Cambridge, UK **2013**.
[57] J. Cui, M. Daboczi, M. Regue, Yi-C Chin, K. Pagano, J. Zhang, M A. Isaacs, G. Kerherve, A. Mornto, J. West, S. Gimenez, Ji-S Kim, S. Eslava, *Adv. Funct. Mater.* **2022**, *32*, 2207136.
[58] F. Le Formal, E. Pastor, S. D. Tilley, C. A. Mesa, S. R. Pendlebury, M. Grätzel, J. R. Durrant, *J. Am. Chem. Soc.* **2015**, *137*, 6629.
[59] M. Barroso, C. A. Mesa, S. R. Pendlebury, A. J. Cowan, T. Hisatomi, K. Sivula, M. Grätzel, D. R. Klug, J. R. Durrant, *Proc. Natl. Acad. Sci. USA.* **2012**, *109*, 15640.
[60] S. Selim, L. Francàs, M. García-Tecedor, S. Corby, C. Blackman, S. Gimenez, J. R. Durrant, A. Kafizas, *Chem. Sci.* **2019**, *10*, 2643.
[61] R. Godin, Y. Wang, M. A. Zwijnenburg, J. Tang, J. R. Durrant, *J. Am. Chem. Soc.* **2017**, *139*, 5216.
[62] K. Maeda, X. Wang, Y. Nishihara, D. Lu, M. Antonietti, K. Domen, *J. Phys. Chem. C.* **2009**, *113*, 4940.
[63] X. Wang, K. Maeda, A. Thomas, K. Takanabe, G. Xin, J. M. Carlsson, K. Domen, M. Antonietti, *Nat. Mater.* **2009**, *8*, 76.
[64] Y. Ma, A. Kafizas, S. R. Pendlebury, F. Le Formal, J. R. Durrant, *Adv. Funct. Mater.* **2016**, *26*, 4951.
[65] Y. Tang, X. Fang, X. Zhang, G. Fernandes, Y. Yan, D. Yan, X. Xiang, J. He, *ACS Appl. Mater. Interfaces.* **2017**, *9*, 36762.
[66] C. Hu, X. Li, C. Dong, B. Li, X. Zhang, W. Sun, Y. Ding, *Mater. Chem. Front.* **2023**, *7*, 5333.
[67] P. Sharma, J.-W. Jang, J. S. Lee, *ChemCatChem.* **2019**, *11*, 157.
[68] M.-J. Choi, T. L. Kim, K. S. Choi, W. Sohn, T. H. Lee, S. A. Lee, H. Park, S. Y. Jeong, J. W. Yang, S. Lee, H. W. Jang, *ACS Appl. Mater. Interfaces.* **2022**, *14*, 7788.
[69] H. Liu, X. Fan, Y. Li, H. Guo, W. Jiang, G. Liu, *J. Environ. Chem. Eng.* **2023**, *11*, 109224.